Discover Applied Sciences

RESEARCH Open Access

An overview on the structure and electrochemical properties of Co-free Ni-rich $LiNi_{0.8}Mn_{0.1}Fe_{0.1}O_2$ as a cathode material for lithium-ion batteries

Rasha S. El-Tawil[1], Somia M. Abbas[1], Ashraf E. Abdel-Ghany[1], Ahmed M. Hashem[1*], Luca Bargnesi[2] and Catia Arbizzani[2]

*Correspondence:
Ahmed M. Hashem
ahmedh242@yahoo.com
[1]Inorganic Chemistry Department, National Research Centre, 33 El Bohouth St., (Former El Tahrir St.), Dokki, Giza 12622, Egypt
[2]Department of Chemistry "Giacomo Ciamician", Alma Mater Studiorum, University of Bologna, Via F. Selmi 2, 40126 Bologna, Italy

Abstract

This study explores and throws more light on a new cobalt-free, nickel-rich $LiNi_{0.8}Mn_{0.1}Fe_{0.1}O_2$ cathode material for lithium-ion batteries. New technique was used to synthesize cobalt-free cathode material by replacing cobalt with iron in the NMC structure. The material is synthesized using a two-step process: first, an oxalate precursor is formed via co-precipitation, followed by a solid-state reaction with lithium hydroxide and iron citrate. The physico-chemical properties of $LiNi_{0.8}Mn_{0.1}Fe_{0.1}O_2$ are analyzed using various techniques, including X-ray diffraction, Raman spectroscopy, scanning electron microscopy, thermal gravimetric analysis, energy dispersive X-ray spectroscopy, and X-ray photoelectron spectroscopy (XPS). Electrochemical performance of the $LiNi_{0.8}Mn_{0.1}Fe_{0.1}O_2$ electrode is evaluated at a C/2 rate within a voltage range of 3.0–4.4 V vs. Li^+/Li and delivers a specific capacity of approximately 80 mAh g^{-1}. The capacity increases to 120 mAh/g after decreasing the current density to C/10 rate within the same voltage range of 3.0–4.4 V vs. Li^+/Li. This relatively new cathode material also shows a good rate capability.

Keywords Co-free, Ni-rich, Cathode, Li–ion batteries, $LiNi_{0.8}Mn_{0.1}Fe_{0.1}O_2$

1 Introduction

Lithium-ion batteries (LIBs) are widely recognized as the primary power source for long-range electric vehicles (EVs). Among the components of these electrochemical devices, the cathode material is the most critical, costly, and heaviest part [1–3]. In the Ni-rich $LiNi_{1-x-y}Mn_xCo_yO_2$ (NMC) and $LiNi_{1-x-y}Co_xAl_yO_2$ (NCA) systems, cobalt is added to stabilize the structure, reduce Li/Ni cation mixing (antisite defects), and enhance thermal stability [4]. However, in the short to medium term, cobalt poses a significant supply chain risk for electric vehicles due to its limited availability and geopolitical concerns [5, 6]. Since raw materials account for 50% to 70% of a battery's cost, the battery industry has recognized the need to reduce or eliminate cobalt from cathode materials without

compromising their performance, driven by societal, economic, and security concerns [7, 8]. Moreover, although cobalt is typically believed to enhance rate performance, several studies have shown that cobalt may be more detrimental than nickel due to chemo-mechanical cracking and irreversible oxygen release at high voltages [9, 10]. As a result, low-cobalt or cobalt-free cathode materials have become a growing trend. In the search for an ideal high-performance cathode, nickel-rich oxides, such as $LiNiO_2$ (LNO), stand out as strong candidates. LNO offers a high theoretical discharge capacity (~ 270 mAh g^{-1}) and a high average potential of 3.8 V vs. Li^+/Li. However, this material presents significant technical challenges for commercial use [11, 12]. Despite over two decades of intensive research, LNO remains difficult to work with due to several major drawbacks: (i) mechanical issues caused by large volume changes (up to ~ 7%), (ii) particle cracking, (iii) multiple phase transitions during cycling, and (iv) surface instability during the delithiation process [13, 14]. To improve safety and high-rate capability, various promising strategies have been developed, including bulk doping and surface passivation. Cobalt-free $LiNi_{1-n}MnO_2$ materials doped with Al, Mn, or Mg (M=Al, Mn, or Mg) have been explored by Dahn et al. [15], who demonstrated that doping $LiNiO_2$ with 5% Al, 5% Mn, or 5% Mg cations effectively suppresses multiple phase transitions during charge and discharge cycles. Sun et al. [16] conducted a thorough comparison of the electrochemical properties and structural stability of $Li[Ni_{0.9}Co_{0.1}]O_2$ (NC90), $Li[Ni_{0.9}Co_{0.05}Mn_{0.05}]O_2$ (NCM90), and cobalt-free $Li[Ni_{0.9}Mn_{0.1}]O_2$ (NM90). They found that Ni-rich $LiNi_{1-x}Mn_xO_2$ cathodes, particularly the NM90, exhibited better cycle stability than their cobalt-containing counterparts, especially under challenging cycling conditions, such as higher cutoff voltages or elevated temperatures. Elmaataouy et al. [7] reported that $LiNi_{0.8}Fe_{0.1}Al_{0.1}O_2$ (NFA), synthesized via a solid-state reaction, delivered high specific capacities of approximately 180 mAh g^{-1} at a 0.1C rate. Additionally, Xi et al. [17] demonstrated that $LiNi_{0.8}Fe_{0.1}Mn_{0.1}O_2$ (NFM) achieved a specific capacity of 202.6 mAh g^{-1} at a 0.1C rate within a 3.0–4.5 V range. Muralidharan et al. [18] found that the cobalt-free $LiNi_{0.85}Fe_{0.052}Al_{0.091}O_2$ material delivers a high capacity of 190 mAh g^{-1} at a 0.1C rate. In a review, Li et al. [19] discussed the phase transition mechanisms of cobalt-free, Ni-rich cathode materials, highlighting existing challenges and advanced characterization techniques used to study phase transitions. They explored the causes of crystal structure degradation, interfacial instability, and mechanical degradation, ranging from the material's crystal structure to its phase transitions and atomic orbital splitting. Ni et al. [20] reported that the single-crystalline, cobalt-free $LiNi_{0.95}Mn_{0.05}O_2$ (NM95) cathode, designed using a molten salt-assisted method, exhibits impressive structural stability and cycling durability. The NM95 cathode achieves a high discharge capacity of 218.2 mAh g^{-1} and a high energy density of 837.3 Wh kg^{-1} at 0.1C, largely due to abundant Ni^{2+}/Ni^{3+} redox. Shen et al. [21] demonstrated that $LiNi_{0.8}Mn_{0.18}Fe_{0.02}O_2$ significantly outperforms the commercially available polycrystalline $LiNi_{0.83}Co_{0.11}Mn_{0.06}O_2$ electrode. It strikes an optimal balance between material cost and electrochemical performance, reducing production costs by more than 15%, while also offering excellent thermal stability and cycling performance. Recently, Kan et al. [22] evaluated the electrochemical performance of $LiNi_{0.94}Mn_{0.04}Al_{0.02}O_2$ (NMA), synthesized via a solid-phase sintering process. NMA exhibited minimal Li^+/Ni^{2+} mixing and retained 79.89% of its capacity at 100th cycle.

In this work, new technique was used to synthesize cobalt-free cathode material by replacing cobalt with iron in the NMC structure. $LiNi_{0.8}Mn_{0.1}Fe_{0.1}O_2$ (NMF811) was synthesized using a co-precipitation process, with oxalic acid serving as a chelating agent. This study provides detailed insights into the structure, composition, morphology, and thermal stability of the prepared sample, using techniques such as X-ray diffraction (XRD), Raman scattering (RS) spectroscopy, scanning electron microscopy (SEM), transmission electron microscopy (TEM), energy dispersive X-ray spectroscopy (EDX), thermogravimetry (TG), and X-ray photoelectron spectroscopy (XPS). The NMF811 cathode demonstrates favorable electrochemical properties while maintaining structural stability, owing to the nearly identical ionic radii of low-spin Ni^{3+} ($r_{Ni^{3+}} = 0.56$ Å) and Fe^{3+} ($r_{Fe^{3+}} = 0.55$ Å). Electrochemical performance of the NMF811 electrode is evaluated through cyclic voltammetry (CV) and galvanostatic charge–discharge (GCD) experiments, showing good cycling stability at 0.2C and strong discharge capabilities at various C rates.

2 Materials and methods

2.1 Materials synthesis

The cobalt-free $LiNi_{0.8}Mn_{0.1}Fe_{0.1}O_2$ cathode material was synthesized using a two-step process, with nickel(II) acetate tetrahydrate (AR), manganese(II) acetate tetrahydrate (AR), iron(III) citrate (AR), and lithium hydroxide (AR) as the starting reagents. In the first step, an oxalate precursor was prepared through co-precipitation. Nickel acetate tetrahydrate and manganese acetate tetrahydrate were dissolved in double-distilled water and then gradually added to a 1 mol/L solution of oxalic acid at 60 °C. After vigorous stirring at 60 °C, the nickel and manganese oxalate precipitate formed. The mixture was then filtered, washed with distilled water, and dried at 100 °C overnight. In the second step, the dried precursor was ground with stoichiometric amounts of $LiOH{\cdot}H_2O$ and iron citrate. The mixture was first calcined at 450 °C for 5 h, then ground and calcined again at 800 °C for 10 h in an ambient air, with intermittent grinding after the initial 5 h. A schematic of the synthesis process, assisted by oxalic acid as a chelating agent, is shown in Fig. 1. For structural and electrochemical comparison, Ni-rich $LiNi_{0.8}Mn_{0.1}Co_{0.1}O_2$ (NMC811) was prepared using the same method, replacing cobalt with $Co(CH_3COO)_2{\cdot}4H_2O$ as the cobalt precursor.

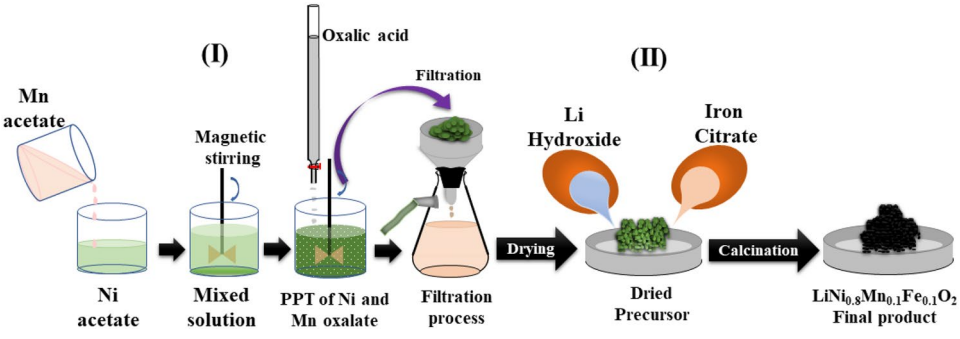

Fig. 1 Schematic diagram of the two-step synthesis process for the Co-free Ni-rich NMF811 cathode material: (I) co-precipitation process aided by oxalic acid as a chelating agent, followed by (II) solid-state reaction of the oxalates with lithium hydroxide and iron citrate

2.2 Materials characterization

The phase composition and structure of the samples were analyzed by XRD using Philips X'Pert apparatus equipped with a CuK_α X-ray source ($\lambda = 1.54056$ Å). Data were collected in the 2θ range 10–80° at a step of 0.05°. The obtained XRD patterns were refined using the FULLPROF software (Toolbar Fullprof suit program (3.00), version June-2015). TGA measurements were carried out using a thermal gravimetric analyzer (Perkin Elmer, TGA 7 series) in the temperature range of 30–1000 °C in air at a heating rate of 10 °C min^{-1}. The surface morphology of the as-fabricated samples was visualized using field emission scanning electron microscopy (Quanta, FEG 250). The microstructure and morphology of the materials were observed with a JEOL 2100F microscope operated at 200 kV and equipped with a Cs corrector to achieve atomic resolution better than 0.14 nm. BET surface area and pore size distribution of synthesized samples were determined from N_2-adsorption experiments using (Belsorp max version 2.3.2). The Brunauer–Emmett–Teller (BET) specific surface area and pore size distribution were calculated from N_2-adsorption experiments using a Belsorp max version 2.3.2 analyzer (Microstac Retsch GmbH, Haan, Germany). Raman scattering (RS) spectra were measured using a micro-Raman-laser spectrometer model Lab-Ram (Horiba-Jobin–Yvon, Longjumeau, France) equipped with 50 × microscope lens, D2 filter, aperture of 400 µm, and a slit of 150 µm. The spectra have been recorded with the 632 nm laser excitation. Thermo Scientific's X-ray photoelectron spectroscopy (XPS, monochromatic AlKα radiation) instrument was used to investigate the samples' surface composition and oxidation states.

Electrode preparation was carried out by adding the powders of active material NMF811 and carbon black (CB) as conductive additive (C65 Carbon black, Imerys Graphite & Carbon) to a polyvinylidene fluoride (PVDF, Kynar HSW 900, > 99%, Arkema) solution in N–Methyl–2–pyrrolidone (NMP, > 99%, Honeywell Fluka). The electrode slurry was prepared with a ratio of 85: 7.5: 7.5 wt% of NMF811, CB and PVDF respectively. The slurry was roll coated onto an aluminum sheet (0.02 mm) previously etched for 2 min in a 5 wt% solution of potassium hydroxide (KOH, ≥ 85%, Merck KGaA). After drying at 60 °C for 24 h, electrodes have been cut and heat treated at 120 °C for 12 h under vacuum in an oven (B–585 Kugelrohr, BÜCHI Labortechnik AG). The obtained NMF811 electrode has an active mass loading in the range 1.5–1.9 mg cm^{-2}. Coin cells (CR2032, stainless steel 312, MTI corp.) and stainless steel T–shaped cells (Swagelok, Swagelok company) have been assembled in a glove box (Mbraun Labmaster SP, MBraun Inc.) in an inert argon atmosphere ($O_2 < 0.1$ ppm and $H_2O < 0.1$ ppm) using NMF811 electrodes as working electrodes (0.636 cm^2), lithium metal (1.13 cm^2, 0.75 mm thick, 99.9% Merck KGaA) with Celgard 2300 as separator, using 1 mol L^{-1} $LiPF_6$ in EC:DMC 1:1 wt% (LP30, Solvionic SA) as the electrolyte solution. Electrodes were electrochemically characterized by cyclic voltammetry (CV) in three electrodes mode, while galvanostatic charge/discharge (GCD) cycles using a potentiostat/galvanostat (VSP, Biologic).

3 Results and discussion

3.1 Structural analysis

Figure 2a shows XRD patterns of the synthesized NMF811 and NMC811 samples. Well-resolved reflections with a very smooth background indicate a high crystallinity of Ni-rich layered oxides. All reflections are indexed to the characteristic Bragg lines of the

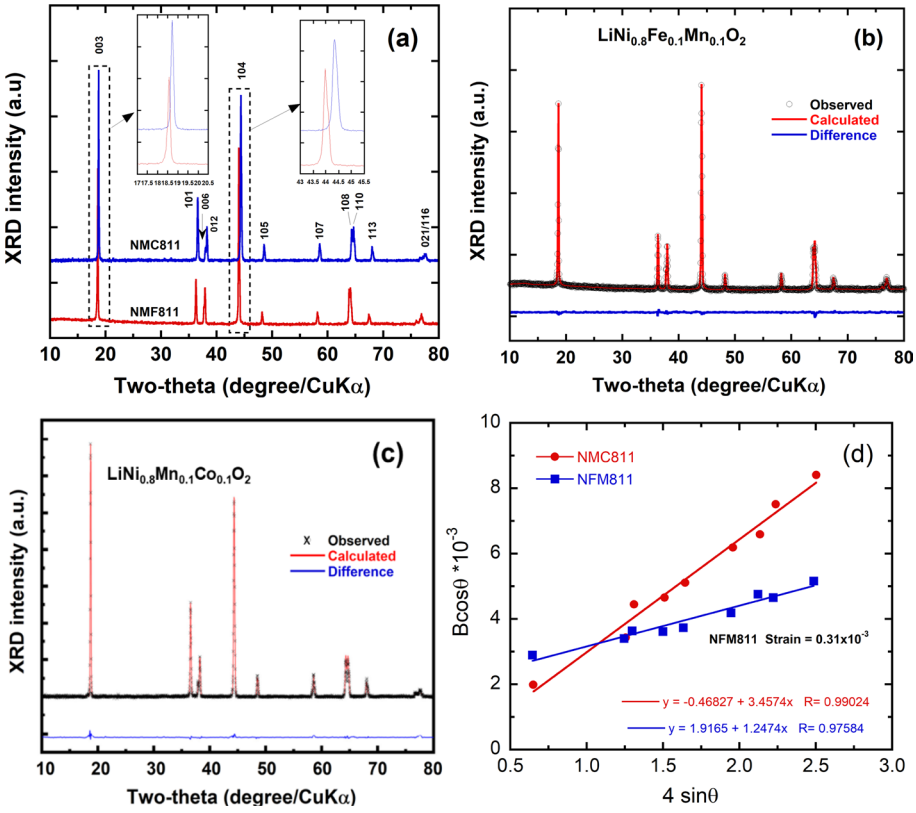

Fig. 2 Structural Properties of Ni-rich Samples: **a** XRD patterns of NCM811 and NMF811 samples obtained using a CuKα X-ray source, **b** Rietveld refinement of the XRD pattern for the NMF811 sample, **c** Rietveld refinement of the XRD pattern for the NCM811 sample, **d** Determination of the microstrain (ε) from the full-width at half-maximum (Bhkl) of XRD reflections, based on Eq. (4)

α-$NaFeO_2$ type structure (*R*-3 *m* space group, JCPDS card No. 82-1495) without any residual impurities or secondary phases. This means that all Fe atoms were incorporated into the crystal α-$NaFeO_2$ type structure without the formation of impurities during the preparation process. A careful analysis of the X-ray diffractogram of the NMF811 sample indicates that the positions of the main peaks are shifted slightly toward the lower-angle region (Fig. 2a) compared to XRD for pure NMC811. This shift confirms that low-spin Fe^{3+} ions with ionic radius (0.55 Å) were introduced into the crystal structure replacing Co^{3+} ions (ionic radius of 0.545 Å) that results in an increase of the *c*-axis parameter [17, 23–25]. Some additional observations are recognized. (i) The $I_{(003)}/I_{(104)}$ intensity ratio which often used to identify the degree of cation mixing between Ni^{2+} ions and Li^{+} ions in Ni-rich NMC oxides, is slightly smaller for the synthesized NMF811 oxide (0.94) compared to Ni-rich NMC oxides. (ii) The (108)/(110) peak splitting, which reflects the well-ordered layered structure, is less evidenced for the NMF811 oxide, which can indicate the occupancy of some Fe^{3+} ions on Li^{+} sites [26–28]. Lattice parameters of as-prepared samples are listed in Table 1. It is important to note that the cubic phase cannot be detected even with an iron content of approximately 10%, as the X-ray reflections from the cubic phase (space group Fm-3 m) overlap with those of the hexagonal phase (space group R-3 m). Additionally, the broadening observed in the XRD reflections, which adversely affects the splitting of the (108)/ (110) pair, can be attributed to the overlapping of the (111), (200), (220), and (311) peaks of cubic $LiFeO_2$ with the (006/012), (104), (108/110), and (021) peaks of the NFM811 oxide.

Table 1 Structural parameters and site occupancy factors derived from the Rietveld refinements of the X-ray diffractograms for the NMC811 and NMF811 samples

Crystal data	NMC811	NMF811
Lattice parameters		
a = b (Å)	2.875 (3)	2.881 (1)
c (Å)	14.221 (7)	14.29 (9)
V (Å^3)	102.13	102.79
c/a	4.94 (6)	4.96 (3)
$I_{(003)}/I_{(104)}$	1.27 ± 0.03	0.94 ± 0.03
2θ position (°)		
< 003 >	18.69	18.56
< 104 >	44.29	44.08
L_c (nm)	55 ± 2	73 ± 2
$\varepsilon \times 10^{-3}$ (rd)	0.86	3.1
Reliability factors		
R_p (%)	9.18	9.83
R_{wp} (%)	11.86	10.45
χ^2	1.24	1.56
Occupancy (%)		
Ni^{2+}on Li-site	5.78	3.79
Fe^{3+}on Li-site	–	2.32
Material fraction (mol%)		
R3m	100	95.8
Fm3m	–	4.2

To characterize the phase purity and composition, the full structural analysis of the NMF811 sample was conducted using Rietveld refinements. Figure 2b, c shows the Rietveld refinements for the NMF811 and NMC811 samples, respectively. In the NMC system, it is known that the presence of Mn^{4+} ions, along with low-spin Ni^{3+} ions in the same transition metal (TM) slabs, leads to charge compensation, resulting in an equal amount of Ni^{2+} ions that are distributed between the TM slabs and the Li inter-slab spaces. When iron is introduced as a substitute, Fe ions cannot exist in a divalent state in the presence of Ni^{3+} [29]. Therefore, the extra TM cations that must be in the Li site will be Ni^{2+} or Fe^{3+}. Considering the respective ionic radii of Li^+ ($r_{Li^+}^{CN=6} = 0.76$ Å), Ni^{2+} ($r_{Ni^{2+}}^{CN=6} = 0.69$ Å), and low-spin Fe^{3+} ($r_{Fe^{3+}}^{CN=6} = 0.55$ Å) [30] in an octahedral environment, it appears that the Li sites are simultaneously occupied by both 3*d* cation $Ni^{2+}$and Fe^{3+} ions [29, 31, 32]. This provides more evidence for the presence of some Fe^{3+} in the Li layer. Therefore, the chemical formula of the Li planes can be written as $\left[Li_{1-x}Ni_{x-y}^{+2}Fe_y^{+3}\right]_{3a}$. Moreover, Fe^{3+} preferentially occupies Li(3*a*) sites compared to Ni^{2+} [31], which sets the constraint $x–y < y$, or $x < 2y$. Therefore, the refinement process was based on fixing the Mn occupancy in transition metal (TM) (*3b*) sites and varying the ratios of the Ni and Fe occupancies on the TM (*3b*) and Li (*3a*) sites, *i.e.,* the *3a* sites are occupied by Li^+, Ni^{2+}, and Fe^{3+}, and the TM ions (Ni, Mn, and Fe) are located at the *3b* sites, while the O^{2-} anions occupy the 6*c* sites. Since the total occupancy of each site *3a* and *3b* should be equal 1, we can propose the chemical formula for the NMF811 sample as follows:

$$\left[Li_{1-x}\ Ni_{x-y}^{+2}\ Fe_y^{+3}\right]_{3a}\left[Ni_{0.7}^{+3}Mn_{0.1}^{+4}\ Fe_{0.1-y}^{+3}\ Ni_{0.1-z+y}^{+2}\right]_{3b}[O_2]_{6c}\,. \quad (1)$$

The Rietveld refinements are presented in Fig. 2b and c. In these Figures, the experimental data are represented by black circles or crosses, while the calculated spectra

are shown as solid red lines. The difference between the calculated and experimental diffractograms, indicated by the blue curves, reflects the quality of the fit, which helps validate the structural model. A strong agreement between the calculated diagrams and observed patterns was achieved for the NMF811 composition, assuming a rhombohedral structure (R-3 m space group), and cubic structure (Fm-3 m S.G.).In the XRD analysis, the phase fraction was refined with an uncertainty of 0.1%, optimizing the fit by minimizing the difference between the experimental and calculated diffractograms. The best Rietveld fit for the NMF811 sample, showing excellent agreement between the calculated and observed patterns, was obtained with 3.79% Ni^{2+}/Li^{+} anti-site defects and 2.32% Fe^{3+}/Li^{+} anti-site defects. Additionally, the analysis revealed the presence of approximately 4.2 mol% of a secondary cubic phase (space group Fm-3 m) coexisting with the primary hexagonal structure (space group R-3 m).

The coherence length (*Lc*) determined using Scherrer's formula is 75 ± 2 nm for NMF811, which represents an increase compared to that of NMC811. This enhancement can be attributed to the substitution of Fe for Co. The crystallity size (*Lc*) and microstrain (ε) of the NMF811 particles were determined using the Williamson-Hall equation [33]:

$$\mathrm{B_{hkl}}\cos\,\theta_{\mathrm{hkl}} = (\mathrm{K}\lambda/\mathrm{Lc}) + 4\varepsilon\,\sin\,\theta_{\mathrm{hkl}} \tag{2}$$

where B_{hkl} represents the line broadening of a Bragg reflection (*hkl*), *K* is the shape factor, L_c is the effective crystallite size and λ is the X-ray wavelength. The microstrain ε is estimated from the slope of the plot B_{hkl} cos θ_{hkl} vs. sin θ_{hkl}, while the intercept on the vertical axis provides the crystallite size (Fig. 2d). The B_{hkl} value used here is corrected for instrumental effect. The calculated miscrostrain for NMF811 is 3.1×10^{-3} rd, which is higher than that of NMC811 (Table 1). This suggests a slight difference in crystallinity between the two materials, with NFM811 exhibiting lower crystallinity compared to NMC811.

Analysis of the data in Table 1 reveals that the *a*- and *c*-lattice parameters of NMF811 have slightly increased by 0.14% and 0.7%, respectively, compared to those of NMC811. This expansion can be attributed to the slightly larger ionic radius of Fe^{3+} (0.645 Å) compared to Ni^{3+}(0.56 Å). As a result, substituting Fe^{3+} for Ni^{3+} leads to a modest enlargement of the crystal lattice. Additionally, the structural refinements assess the Li–O and TM–O bond lengths, as well as the thicknesses of the TM intraslab (i.e., metal–O_2 plane) denoted as $S_{(MO2)}$ and the interslab (LiO_2) thickness represented by $I_{(LiO2)}$, expressed as [34]:

$$S_{(\mathrm{MO2})} = 2\,(1/3 - Z_{oxy})\,c, \tag{3}$$

$$I_{(\mathrm{LiO2})} = c/3 - S_{(\mathrm{MO2})}. \tag{4}$$

The results are presented in Table 2. It can be observed that the values for $S_{(MO2)}$ and $I_{(LiO2)}$ have slightly increased by 1.1% and 0.5%, respectively, compared to those of the NMC811 sample [3]. This suggests the presence of Fe^{3+} ions ($r_{Fe^{3+}}^{CN=VI}$ = 0.645 Å) at both the Li(3*a*) and TM(3*b*) sites [25, 35]. The incorporation of Fe^{3+} ions at the Li(3a) site helps reduce the Li/Ni cation mixing. Specifically, the percentage of Ni^{2+} ions in the Li(3a) site (3.79%) for NMF811 is lower than that observed in pristine NMC811 (5.57%), further supporting the beneficial effect of Fe^{3+} ions at the Li(3a) site. Additionally, the

Table 2 Bond lengths and slab thickness for NMF811 sample, compared with data obtained from literature

Material	Bond length (Å)		Slab thickness (Å)	
	Li–O	TM–O	Intraslab $S_{(MO2)}$	Interslab $I_{(LiO2)}$
NMC811	2.1135 (1) [19]	1.966 (2) [19]	2.114 (2)	2.622 (1)
NMF811	2.1150(2)	1.998(3)	2.137 (2)	2.635(7)

refinement indicates that the actual formula of the final sample is represented by Eq. (1), with x ≃ 0.0379 and y ≃ 0.0232. Thus, the value of x = 0.0611, and the final formula is as follows:

$$\left[\mathrm{Li}_{0.9389}\mathrm{Ni}^{2+}_{0.0379}\mathrm{Fe}^{3+}_{0.0232}\right]_{3a}\left[\ \mathrm{Ni}^{3+}_{0.6988}\mathrm{Mn}^{4+}_{0.0986}\mathrm{Fe}^{3+}_{0.0808}\mathrm{Ni}^{2+}_{0.0607}\right]_{3b}\left[\mathrm{O}_2\right]_{6c}.$$

While the total cation mixing ratio ((Ni + Fe)/Li) increases due to the presence of $Fe3^+$ and $Ni2^+$ in the Li(3b) sites (Table 1), negatively impacting the $I_{(003)}/I_{(104)}$ intensity ratio and (108)/(110) peak splitting [29], the incorporation of $Fe3^+$ into lithium sites further degrades electrochemical performance through two key mechanisms. First, although the Ni/Li disorder decreases from 5.78% (NMC811) to 3.79% (NMF811), indicating reduced $Ni2^+$ occupancy in Li sites, this also diminishes the pool of $Ni2^+$ ions that could otherwise participate in the discharge process. Second, $Fe3^+$ substitution stabilizes the lattice in the $Ni2^+$ state (as reported by Prado et al. [36], reducing the availability of electrochemically active $Ni3^+$ and lowering the reversible capacity. Additionally, $Fe3^+$ disrupts the ideal cation distribution, leading to a 6.11% reduction in active lithium content. This loss directly impairs lithium diffusion kinetics and charge capacity. Although the expanded interlayer spacing (LiO_2) and longer Li–O bonds (Table 2) could theoretically facilitate Li^+ hopping [37, 38], these benefits are outweighed by the detrimental effects of $Fe3^+$, including:

- Reduced $Ni3^+/Ni4^+$ redox activity,
- Increased lattice strain from $Fe3^+$'s larger ionic radius, and
- Blocked Li^+ pathways due to cation mixing.

Consequently, significant $Fe3^+$ incorporation in NMF811 compromises its electrochemical performance compared to NMC811."

3.2 Thermal characterization

As reported by Cui et al. [39], thermal runaway in batteries is primarily caused by the thermal decomposition of electrode materials, with Ni-rich materials being particularly susceptible. These authors also noted that Ni-rich cathodes, when in contact with the electrolyte, can undergo thermal decomposition at temperatures as low as 180–190 °C, releasing over 1000 J/g of heat. Furthermore, Ni-rich materials exhibit significant outgassing compared to other cathode materials, such as $LiFePO_4$ (LFP) and $LiMn_2O_4$ (LMO), which react more slowly with the electrolyte. Therefore, enhancing the thermal stability of Ni-rich cathode materials is crucial.

To the best of our knowledge, this is the first investigation into the thermal analysis of NMF811. The TGA curve for the synthesized NMF811 material (Fig. 3) demonstrates good thermal stability, with no significant weight loss observed before 400 °C. A slight weight loss was noted above 400 °C, reaching approximately 1% at 875 °C. Beyond this temperature, additional minor weight loss began, likely due to the decomposition of the

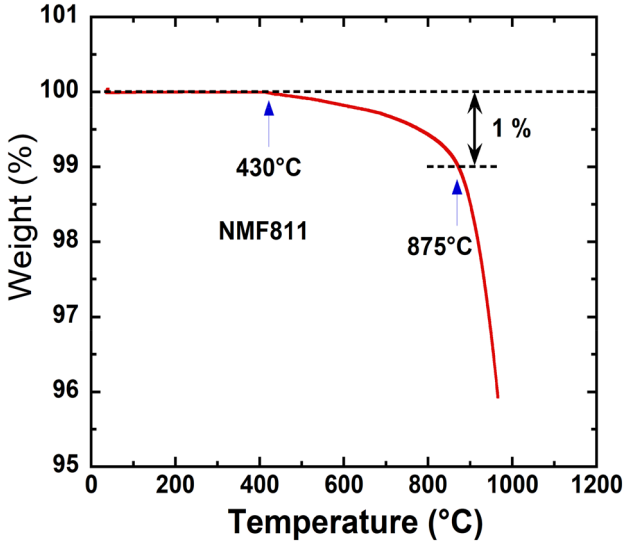

Fig. 3 Thermogravimetric analysis of NMF811 carried out in ambient atmosphere

synthesized material and the thermal volatilization or release of lithium. The thermal behavior of this synthesized NMF811 material is comparable to, or better than, that of NMC811 synthesized by Li et al. [40], where gradual weight loss was observed upon heating until decomposition occurred at 750 °C. This suggests that the complete substitution of Co with Fe may delay the decomposition process. A similar phenomenon has been observed in $LiNi_{0.8}Co_{0.15}Al_{0.05}O_2$ (NCA), likely due to the high bonding energy (low covalency) of Al [39]. It appears that Fe plays a similar role in enhancing the thermal stability of the α-$NaFeO_2$ type structure.

3.3 Morphological characterizations

The morphology of the NMF811 powders was analyzed using SEM and TEM. The SEM images in Fig. 4a, b show that the combination of co-precipitation and solid-state methods influences the morphology of the prepared material. It is clear that the particles are faceted, with smooth surfaces and clean edges. Further investigation of the microstructure of the Co-free NMF811 particles at various magnifications was conducted using TEM (Fig. 4c and d) and SAED (inset of Fig. 4d). From Fig. 4c, the particle size distribution ranges from 50 to 95 nm. The HRTEM image (Fig. 4d) distinctly shows lattice fringes with an interplanar spacing of approximately 0.204 nm, which corresponds to the (104) planes of layered $LiNi_{0.8}Co_{0.1}Mn_{0.1}O_2$. The SAED pattern matches the typical diffraction spots of the R-3 m space group [41].

3.4 Compositional analysis

In addition to Rietveld refinement, energy dispersive X-ray spectroscopy (EDX) was employed to determine the composition of the NMF811 sample. The EDX spectrum shows Lα peaks in the 0.65–0.85 keV range, while Kα peaks are observed between 5.6–7.7 keV. As illustrated in Fig. 5, the spectrum includes peaks corresponding to the Kα electron shell (~6.4 keV) and the Lα shell (~0.7 keV) of iron. The experimental composition of the as-prepared NMF811, derived from the EDX analysis, is $LiNi_{0.7801}Mn_{0.1096}Fe_{0.1101}O_2$. The deviations in the Ni, Fe, and Mn content do not

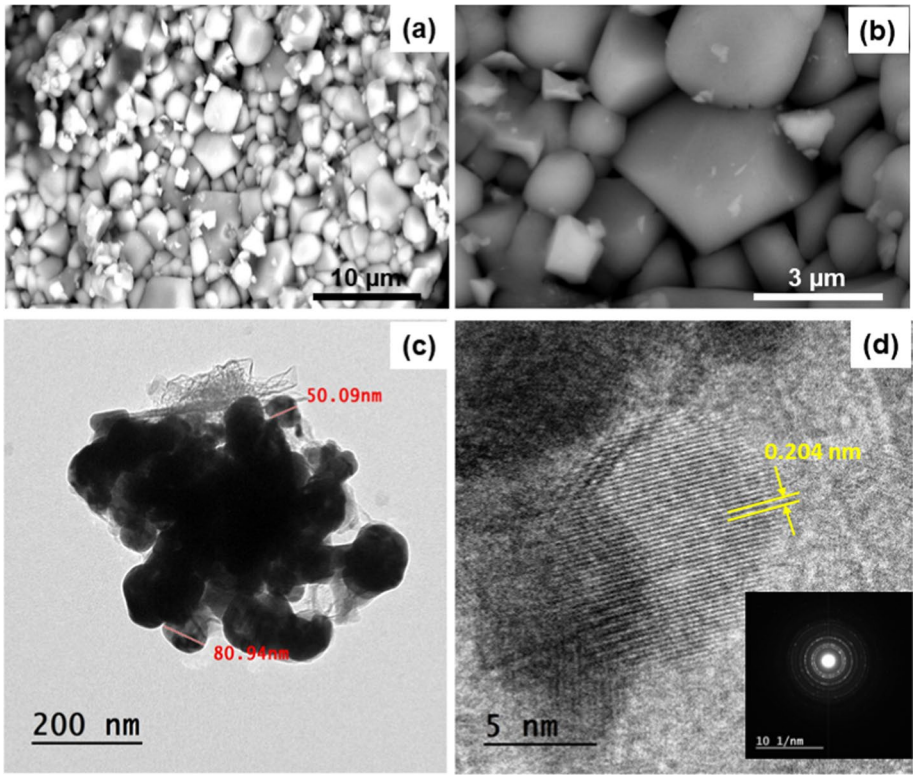

Fig. 4 **a**, **b** SEM images and **c**, **d** HRTEM images of the NMF811 sample prepared by the two-step process including co-precipitation and solid-state reaction

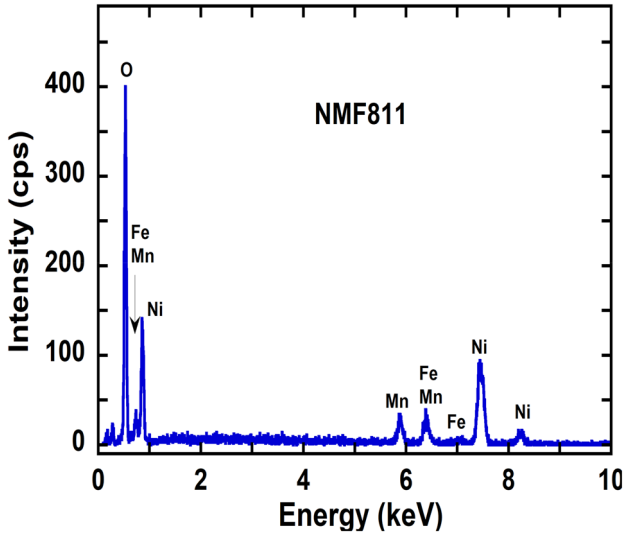

Fig. 5 EDX analysis of the NFM811 sample

exceed 1.0%, indicating a strong agreement between the EDX results and the Rietveld refinement.

3.5 Raman spectroscopy

Due to its sensitivity to the short-range oxygen coordination around cations in oxide frameworks, Raman spectroscopy was used to explore the structural characteristics of

the synthesized NMF811. The atomic motion of cations towards their oxygen neighbors, make them highly responsive to the cationic local environment in the rhombohedral crystal lattice [27]. Layered NMC compounds exhibit D_{3d}^5 spectroscopic symmetry, and the Raman active vibrational modes associated with three transition-metal ions are represented as $\Gamma = 3A_{1g} + 3E_g$, where A_{1g} and E_g species originate from M–O stretching and O–M–O bending vibrations, respectively [37]. The best fit of the Raman spectrum, starting from a prescribed set of six individual bands of Lorentzian shape that overlap to give rise to the two broad A_{1g} and E_g features as shown in Fig. 6. The sets of Lorentzian bands for Ni, Fe and Mn ions, are centered at 468, 524 and 598 cm^{-1} for the E_g species and at 562, 656 and 695 cm^{-1} for the A_{1g} species, respectively. Note that the A_{1g} mode has greater oscillation strength and therefore exhibits higher peak intensity. For $LiNiO_2$ and for $LiMnO_2$ the Raman peaks attributed to the A_{1g} and E_g modes are located at 544, 465 cm^{-1} and at 605, 479 cm^{-1}, respectively [17]. It is obvious that these vibrational features are consistent with the formation of the $LiNiO_2$-$LiMnO_2$-$LiFeO_2$ solid solution [7, 42, 43]. For $LiNi_{0.8}Mn_{0.1}Fe_{0.1}O_2$, we observe a significant increase of the Ni mode frequency by several cm^{-1}, which can be attributed to the fact that Ni occurs in two different oxidation states in NMF811 (Eq. 1). The shift in the Mn mode frequency is due to the oxidation state + 4 of Mn ions. Additional vibrational modes appear in the spectra at 408, 533, 653, and 702 cm^{-1}, corresponding to vibrations allowed by the *Fm3m* symmetry of the NaCl-like cubic structure, which overlap with the rhombohedral features. This phase is characterized by five distinct bands at 378, 404, 540, 636, and 704 cm^{-1}, associated with the *F1g* and *F2g* species of the cubic phase [27]. Similar vibrational modes have also been observed in the spectrum of α-$LiFeO_2$ [44]. The most intense peaks at 533 and 653 cm^{-1} are attributed to O–Fe–O bending and Fe–O stretching within the FeO_6 octahedral units. Additionally, two extra bands are observed in Fig. 6: (i) a low-frequency band at 185 cm^{-1}, attributed to the Li-cage mode. The frequency shift in this mode can be attributed to cation mixing caused by the presence of Fe ions at lithium sites, which aligns well with the XRD data. (ii) A high-frequency broad peak, assigned to the second-order Raman band (Table 3).

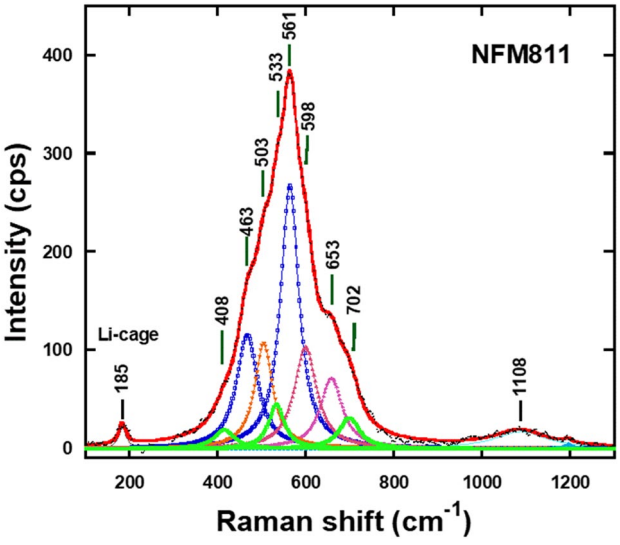

Fig. 6 Typical spectral deconvolution of the Raman pattern of NMF811

Table 3 Analysis of all Raman active modes for NMF811 sample using Lorentzian profiles

Modes		Band position (cm^{-1})	Band width (cm^{-1})	Band area
v_1	Li-cage	185	19	663
v_2	E_g (Ni)	468	68	15,669
v_3	A_{1g} Ni)	562	56	30,218
v_4	E_g (Fe)	524	57	5300
v_5	A_{1g} (Fe)	656	48	3242
v_6	E_g (Mn)	598	55	5682
v_7	A_{1g} (Mn)	695	42	3084
v_8	2nd order	1018	124	2556

Band positions are given with an accuracy of ± 1 cm^{-1}

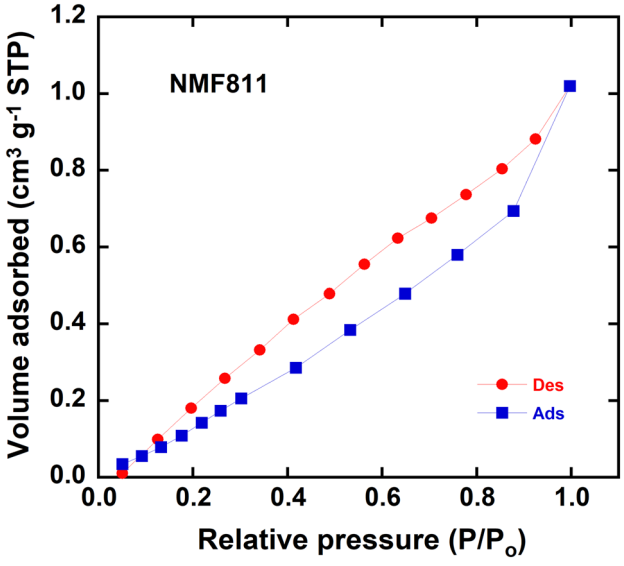

Fig. 7 BET experiments showing N_2 adsorption–desorption isotherms of NMF811

3.6 Specific surface area characterization

The specific surface area (SSA) of an electrochemically active material is a key parameter for determining the exchange current at the electrolyte–electrode interface and the kinetics of Li^+ ions within the electrode. The SSA of the NMF811 powders was measured using the nitrogen adsorption method, and the results are shown in Fig. 7. The isotherm curve for the NMF811 sample exhibits a hysteresis loop, indicating a hierarchical nanoporous structure in the powders. The isotherm increases with rising p/p_o and forms a H3-type hysteresis loop up to $p/p_o \approx 1.0$, according to the IUPAC classification [45]. The BET-specific surface area (S_{BET}) of NFM811 is 8.63 m^2/g, compared to 1.13 m^2/g for NMC811 oxide, reflecting a significant increase in surface area that enhances the transfer of Li^+ ions into the secondary particles. The average nanopore size of 2.4 nm, calculated using the Barrett–Joyner–Halenda (BJH) model, corresponds to the interconnecting voids between the randomly packed nanoparticles within secondary particles. The equivalent particle size (L_{BET}) of 76 nm was calculated from BET measurements using the relationship $A = 3/(\rho L_{BET})$, where A is the specific surface area and ρ is the density (4.6 g/cm^3 for NMF811) [46]. A good agreement is observed between the particle size values of L_{BET} and L_{TEM}. Additionally, the NMF811 powder displays open porosity,

which ensures better wettability and improved electrolyte penetration, leading to shorter diffusion paths in the cathode material and promoting Li^+ transport.

3.7 X-ray photoelectron spectroscopy (XPS) characterizations

The surface elemental composition and valence state of samples are analyzed by X-ray photoelectron spectroscopy. Figure 8a shows the XPS survey spectrum and high resolution XPS (HR-XPS) patterns of the Ni 2p, Mn 2p, Fe 2p and O 1 s core levels for the sample. The binding energies (BE) obtained in the XPS analysis were corrected for specimen charging by referencing the C1s line to 284.20 eV. The survey spectrum (Fig. 8a) indicates the presence of Ni, Mn, Fe, Li and O elements in the NMF811 sample. The XPS spectra were analyzed by evaluating the peak area of elements using Gaussian profiles after removing the secondary electron background. The Ni 2p spectrum (Fig. 8b) shows

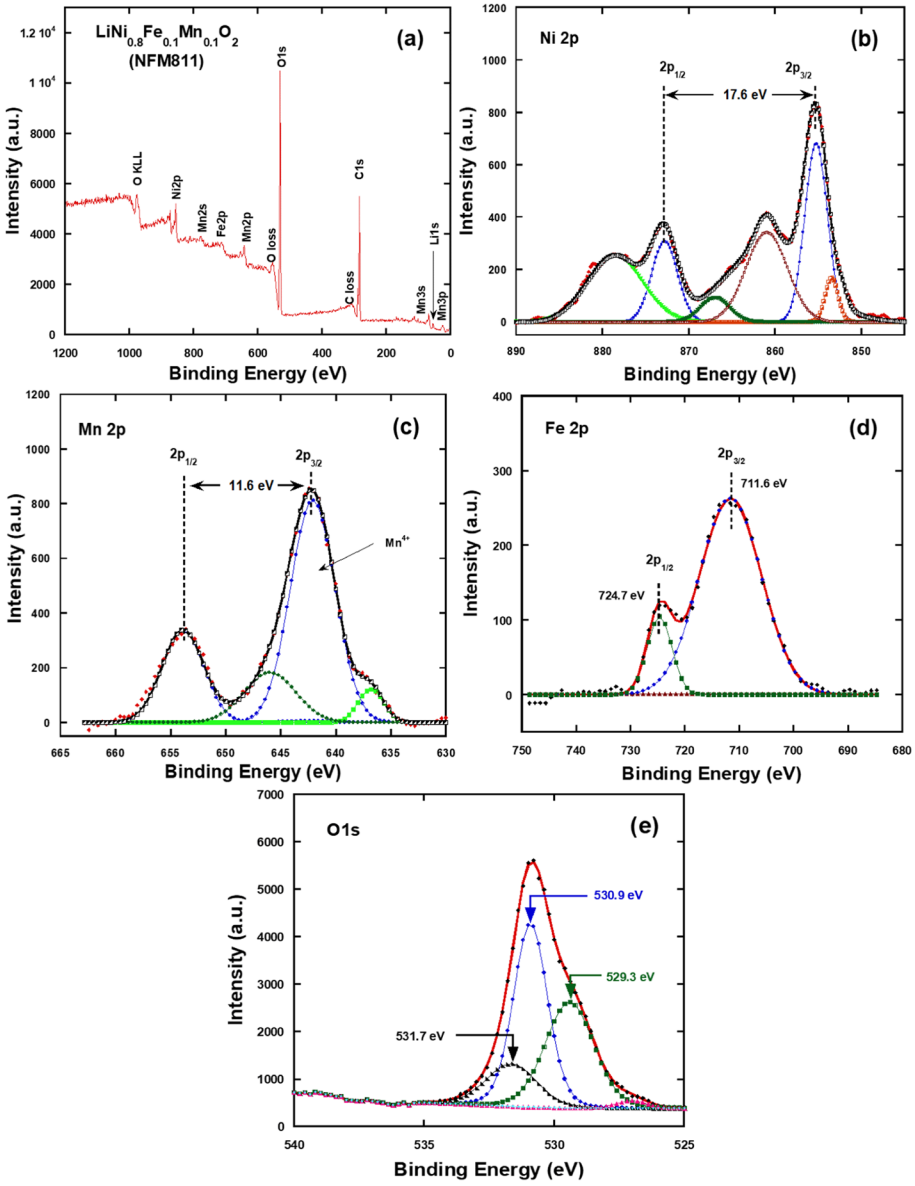

Fig. 8 XPS results for the NFM811 sample. **a** Survey spectra and **b**–**e** high-resolution spectra. **b** Ni 2p, **c** Mn 2p, **d** Fe 2p, and **e** O1s core-level

that the most intense Ni 2p3/2 peak, located at BE of 855.3 eV, is accompanied by a satellite at about 860.9 eV, while Ni 2p1/2 and its satellite are located at 872.9 and 878.6 eV, respectively. The binding energy at BE of 853.5 and 855.3 eV is assigned to Ni^{2+} and Ni^{3+}, respectively (Fig. 8b) respectively, which agree well with those previously reported for Ni^{2+} and Ni^{3+} for NMC811 electrode [23]. Analysis of the Mn 2p core level (Fig. 8c) evidences that the two main characteristic peaks assigned to Mn 2p3/2 and Mn2p1/2 orbitals located at about 642.2 and 653.8 eV, respectively, with 11.6 eV spin–orbit energy separation suggests that the Mn exist in this sample as + 4 valance state which is in good agreement with the values reported previously [23, 35]. Figure 8d presents the HR-XPS spectra of Fe 2p core levels, in which the peaks located at BE of 711.6 and 724.7 eV are attributed to the Fe 2p3/2 and Fe 2p1/2 orbitals, respectively, indicating that Fe in NFM811 sample is present in the form of + 3[17, 45], which is in good agreement with the XRD data. The HR-XPS spectrum of O 1 s core level (Fig. 8e) revealed different types of oxygen, with characteristic peaks at 529.3 eV, 530.9 eV and 531.7 eV ascribed to the transition metal–oxygen (M–O) bonds and the residual oxygen related to impurities with OH- or O- bonding on the surface.

3.8 Electrochemical characterizations

Electrochemical assessments on the as-prepared sample NMF811 were performed in CR2032 coin-type cells using cyclic voltammetry and galvanostatic charge–discharge experiments. The voltammograms carried out at the scan rate of 0.01 mV s^{-1} in the potential range 3.0–4.5 V vs. Li^+/Li are shown in Fig. 9a, which reveal the electrochemical behavior during Li-ion intercalation/deintercalation associated with the corresponding crystallographic transitions. Three pairs of anodic and cathodic peaks located at around 3.70, 3.95, and 4.20 V correspond to $Ni^{2+/3+,4+}$ redox processes and to the phase transition of hexagonal (H1) to monoclinic (M), monoclinic (M) to hexagonal (H2), and hexagonal (H2) to hexagonal (H3), respectively [17, 26, 47, 48]. As shown in Fig. 9a, the anodic peak located at 3.8 V exhibit a slight shift to 3.75 V after the 1st cycle. The voltage difference (ΔV) between anodic and cathodic peaks during the second and the third cycle is stabilized, which gives a good indication about improvement in cycle performance upon cycling. It is worth noting that the cyclic voltammograms of NMF811 are rather different from those NMC811 illustrated in Fig. 9b for which the anodic peak at 4.06 V is shifted to 3.84 V after the 1st cycle.

Figure 9c presents the room-temperature galvanostatic charge/discharge tests of the NMF811 electrode performed at high rate of (C/2 or 0.5C) within the potential range 3.0–4.4 V vs. Li^+/Li. The NMF811 electrode delivers an initial charge and discharge specific capacities of 108 and 79 mAh g^{-1}, respectively, giving an irreversible capacity of 29 mAh g^{-1} and an initial Coulombic efficiency (ICE) of 73%. This looks better than pristine NMC811, which exhibits an irreversible capacity of 50 mAh g^{-1} and an ICE of 71% at lower current density of 0.1C [23]. This improved electrochemical performance may be explained by the interlayer linear Ni^{2+}–O_2–Fe^{3+} generated when Co is completely replaced by Fe maintaining the layered structure of $LiNi_{0.8}Mn_{0.1}Fe_{0.1}O_2$. This ternary layered oxide electrode material mitigates the 180° Ni^{2+}–O^{2-}–Ni^{2+}/Mn^{4+} linear super exchange effect alleviating or retarding Ni/Li mixing, which increases the diffusion rate of Li^+ [49, 50]. Additionally, as observed by Ryu et al. [51] and Yang et al. [52], the full substitution of Co-by-Fe in the NMC811 cathode assists to avoid the detrimental

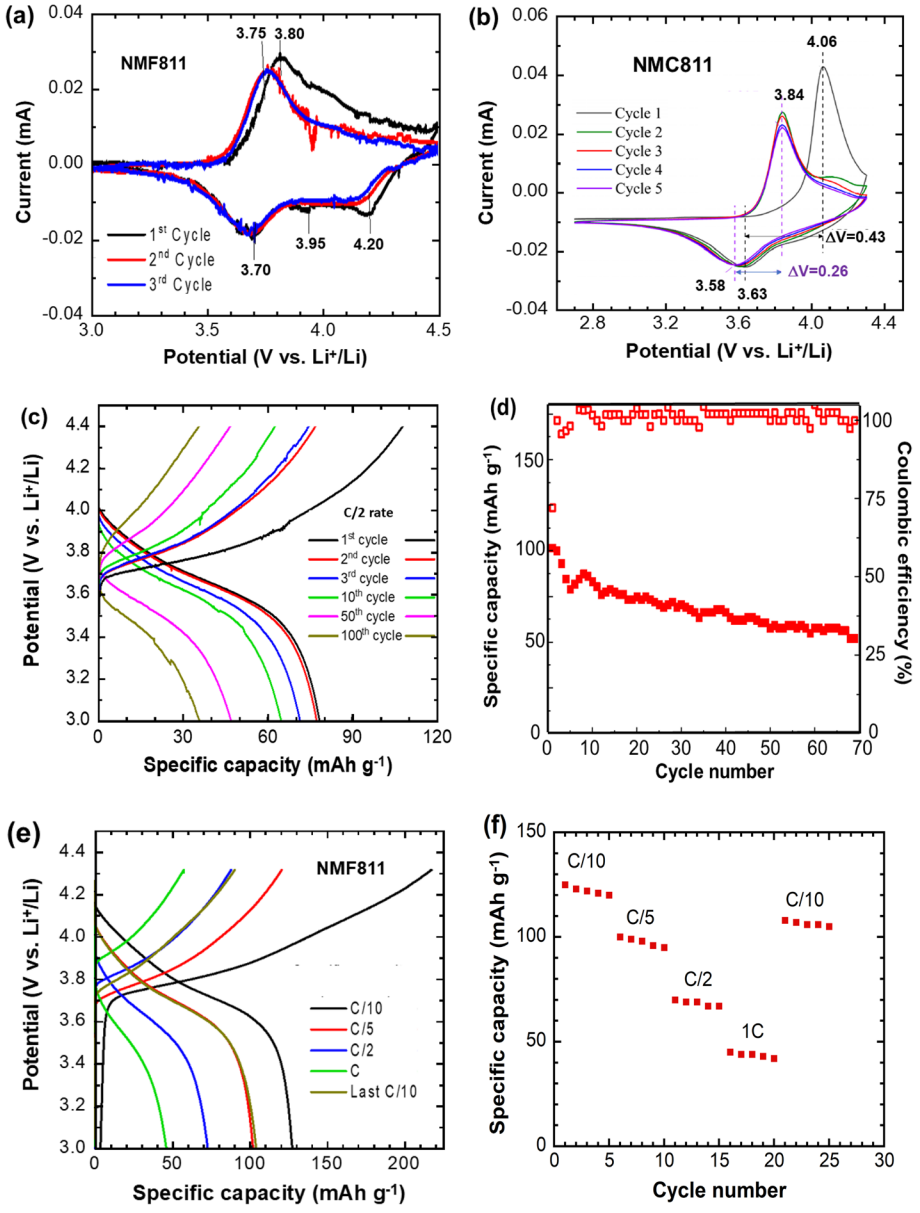

Fig. 9 Electrochemical characterization of the layered oxide electrode. **a** CV profile of NMF811 and **b** CV profile of NMC811 recorded at low sweep rate of 0.01 mV s^{-1} in the potential range 3.0–4.5 V vs. Li^+/Li. **c** GCD profiles of the NMF811 electrode recorded at C/2 rate in the voltage range 3.0–4.4 V. **d** Cycleability of the NMF811 electrode tested at C/5 rate in the potential range 3.0–4.4 V. **e** GCD profiles of the NMF811 electrode recorded at different C-rate. **f** Rate capability of the NMF811 electrode

effect of the H2→H3 phase transition at the end of the charge-process, which considerably affects its cycle stability. Hu et al. reported the mechanism of side reaction inducing capacity fading of Ni-rich cathode [53]. This phase transition causes expansion and contraction of crystal structure, which is closely related to cracks in grains that cause lattice distortion and induce internal strain accelerating the degradation of layered cathode material via an irreversible phase transition (IPT) from layered structure to spinel phase and NiO-like phase.

Figure 9d illustrates the cycleability of the NMF811 electrode tested in the same potential window 3.0 V–4.4 V over 70 cycles at (C/5 or 0.2C) rate. Using this lower C-rate, the

electrode delivers an initial discharge capacity to 102 mAh g^{-1} (ICE 72%) and retained 52 mAh g^{-1} at 70th cycle with capacity retention of 51% (CE ≅ 100%). This improvement in Coulombic efficiency may be ascribed to the incorporation of Fe that maintains the stability of the layered rhombohedral structure and inhibits the transition to a spinel-like structure, which ultimately results in the cubic rock-salt phase [54]. Furthermore, even in the extreme case of a high charging cut-off voltage, Fe doping prevents the local collapse of LiO_2 interslab space during cycling. In order to evaluate the rate capability of the NMF811 cathode, galvanostatic charge–discharge experiments were carried out at various C-rates in the range 0.1C–1C (Fig. 9e and f). It is noted that the discharge capacities of NMF811 at 0.1C, 0.2C, 0.5C, 1.0C are 126, 101, 72, 46 and 103 mAh g^{-1}, respectively. This is another evidence for the possibility to rely on this new electrode material after further modification. It is also worthnoting that the irreversible capacities decrease upon increasing the current densities or C-rate values. This can be well noticed from the comparison of initial capaciteies of C/2 (Fig. 9c) and C/10 (Fig. 9e). In Fig. 9c with C/2, the NMF811 electrode delivers an initial charge and discharge specific capacities of 108 and 79 mAh g^{-1}, respectively, giving an irreversible capacity of 29 mAh g^{-1} and an initial Coulombic efficiency (ICE) of 73%. On the other hand in Fig. 9e with C/10, the NMF811 electrode delivers an initial charge and discharge specific capacities of 213 and 125.5 mAh g^{-1}, respectively, giving an irreversible capacity of 87.5 mAh g^{-1} and an initial Coulombic efficiency (ICE) of 58.9%. This may attribute to the low conductivity of the cubic phase of $LiFeO_2$ which represents about 4.2% (Table 1) of the synthesized sample and also affects its entire capacity. Consistent with reports by Prado et al. [36], the substitution of Fe for Ni in layered oxides stabilizes Ni^{2+} at the expense of electrochemically active Ni^{3+}, while lattice expansion (evidenced by increased a- and c-parameters in Table 1) impedes Li^+ diffusion. These effects collectively degrade capacity retention in NMF811 compared to NMC811.

Fe^{3+} is an active cation that mitigates in occupying the position of Ni^{2+} so it reduces the degree of cation mixing between Ni/Li ions and increases the interlattice region between the layers. So, an increase in the diffusion coefficient of lithium ($D_{Li}+$) in the oxide framework is expected with iron doping. In one side, Fe^{3+} lowers Li^+/Ni^{2+} disordering due to the comparable ionic radius of Ni^{2+} ion (0.69 Å) to Li^+ ion (0.76 Å) by the modification in TM slabs and Li slabs [55]. As Fe^{3+} ions located in transition metal layers (3*b* sites) can easily migrate and occupy into LiO_2 layers (3*a* sites) simultaneously along with Ni^{2+}, therefore, it could be predicted that parts of Fe^{3+} and Ni^{2+} ions reside in the 3*a* sites and hence it reduces the antisite of Ni^{2+} and the cation mixing is reduced (as evidenced from XRD section), this means that more Ni^{2+} participated in the discharge reaction, so as to obtain more specific discharge capacity. On the other side, Fe^{3+} ameliorate the lithium diffusion kinetics as reported by Mofid et al. [56], Fe^{3+} and Co^{3+} have the same role as they have the electronic configuration of ($t_{2g}^5 e_g^0$) and ($t_{2g}^6 e_g^0$), respectively, with almost similar ionic radius, i.e., 0.55 Å for low-spin Fe^{3+} and 0.545 Å for Co^{3+}. So, upon the replacement of Co by Fe ion the *a*-axis and *c*-axis became slightly larger and hence decreases the lithium diffusion barrier. Moreover, the high bond energy of Fe–O (390.4 kJ) lessens oxygen release and increases the lamellar layer structural stability from suffering phase transitions via occupying transition metal (TM) sites [57].

Table 4 highlights the key similarities and differences between NMF811 and commercial $LiNi_{0.8}Co_{0.1}Mn_{0.1}O_2$ (NCM811) and $LiNi_{0.8}Co_{0.15}Al_{0.05}O_2$ (NCA). From this table

Table 4 Comparison of NMF811 with widely studied commercial high-nickel cathodes (NCM811 and NCA)

Property	NFM811 (This Work)	NCM811 [58]	NCA [58]
1. Composition	$LiNi_{0.8}Mn_{0.1}Fe_{0.1}O_2$	$LiNi_{0.8}Co_{0.1}Mn_{0.1}O_2$	$LiNi_{0.8}Co_{0.15}Al_{0.05}O_2$
2. Cobalt content	0%	10%	15%
3. Dopants	Fe, Mn (abundant, eco-friendly)	Co, Mn	Co, Al
4. Environmental impact	Low (Co-free, Fe is eco-friendly)	Moderate	High
5. Sustainability	High (Co-free, Fe is abundant)	Moderate	Low
6. Structural stability	Improved via Fe substitution	Moderate	High, with Al contribution
7. Thermal stability	Good (Fe improves safety)	Moderate	High
8. Synthesis simplicity	Moderate (Fe requires optimization)	Well-established	Well-established
9. Commercial maturity	Emerging/research	Commercial	Commercial

it seems that this Co- free structure ($LiNi_{0.8}Mn_{0.1}Fe_{0.1}O_2$) with further modification in synthesis process can be a good alternative candidate for the commercial ones like $LiNi_{0.8}Co_{0.1}Mn_{0.1}$ (NCM811) and $LiNi_{0.8}Co_{0.15}Al_{0.05}O_2$ (NCA). From this table it can be emphasized that this Co-free structure is a comparative cathode material for the current commercial ones in terms of structure, cost, sustainability and environmental impact. Further modifications will improve its electrochemical performance of capacity retention and rate capability.

4 Conclusion

In this work, a Ni-rich Co-free oxide cathode has been designed by substituting Fe for Co. The compound $LiNi_{0.8}Mn_{0.1}Fe_{0.1}O_2$ was synthesized via a two-step process: the formation of an oxalate precursor by co-precipitation followed by a solid-state reaction with lithium hydroxide and iron citrate. Two structural modifications can be observed upon iron substitution for cobalt: (i) a change in the TM layer spacing and (ii) a shift in the c/a ratio which ascribes to change in the anti-site defect concentration. However, as the ionic radius of low-spin Fe^{3+} (0.55 Å) is not substantially different than that of Co^{3+} (0.545 Å), the shift if the c/a ratio is expected to reflect primarily change in the anti-site defect concentration in the NMF811 material. More importantly, the mechanical inner strain is alleviated by the improved reversible H2-H3 phase transition, which can reduce the formation of cracks and improve the safety performance during long-term cycling. This Ni-rich Co-free cathode material can deliver a specific capacity of ~ 80 mAh g^{-1} and retain about 45% of its initial capacity a 100 cycles at C/2 rate.

Acknowledgements
The authors would like to thank Prof. Dr. C. M. Julien for his sincere help in completing this work.

Author contributions
Conceptualization, A.M.H. and C.A.; methodology, A.E.A.; formal analysis, R.S.E, S.M.A, A.E.A., and L.B.; investigation, R.S.E, S.M.A, A.E.A., and L.B.; data curation, A.E.A.; writing—original draft preparation, A.E.A and A.M.H.; writing—review and editing, A.M..; supervision, A.M.H and C.A.; funding acquisition, A.M.H. All authors have read and agreed to the published version of the manuscript.

Funding
This research was funded by the Egyptian Science, Technology, and Innovation Funding Authority (STIFA, STDF previously) through project number 42691 entitled (Microstructure-Based, Multi-Physics Simulation and Optimization to Improve Battery Performance).

Data availability
All data are provided in this article.

Declarations

Ethical approval and Consent to participate
Not applicable.

Consent to publish
The authors declare that they agree to publish this manuscript after accepting.

Competing interest
The authors declare that they have no known competing financial interests or personal relationships that could have appeared to influence the work reported in this paper.

Received: 9 April 2025 / Accepted: 12 June 2025
Published online: 21 August 2025

References

1. Mizushima K, Jones PC, Wiseman PJ, Goodenough JB. Li_xCoO_2 (0 < x< -1): a new cathode material for batteries of high energy density. Mater Res Bull. 1980;15:783–9. https://doi.org/10.1016/0025-5408(80)90012-4.
2. Ryu HH, Park NY, Seo JH, Yu YS, Sharma M, Mücke R, Kaghazchi P, Yoon CS, Sun YKA. highly stabilized Ni-rich NCA cathode for high-energy lithium-ion batteries. Mater Today. 2020;36:73–82. https://doi.org/10.1016/j.mattod.2020.01.019.
3. Sun HH, Kim UH, Park JH, Park SW, Seo DH, Heller A, Mulli CB, Yoon CS, Sun YK. Transition metal-doped Ni-rich layered cathode materials for durable Li-ion batteries. Nat Commun. 2021;12:6552. https://doi.org/10.1038/s41467-021-26815-6.
4. Liu W, Oh P, Liu X, Lee MJ, Cho W, Chae S, Kim Y, Cho J. Nickel-rich layered lithium transition-metal oxide for high-energy lithium-ion batteries. Angew Chem Int Ed. 2015;54:4440–57. https://doi.org/10.1002/anie.201409262.
5. Yan P, Zheng J, Chen T, Luo L, Jiang Y, Wang K, Sui M, Zhang JG, Zhang S, Wang C. Coupling of electrochemically triggered thermal and mechanical effects to aggravate failure in a layered cathode. Nat Commun. 2018;9:2437. https://doi.org/10.1038/s41467-018-04862-w.
6. Yan P, Zheng J, Liu J, Wang B, Cheng X, Zhang Y, Sun X, Wang C, Zhang JG. Tailoring grain boundary structures and chemistry of Ni-rich layered cathodes for enhanced cycle stability of lithium-ion batteries. Nat Energy. 2018;3:600–5. https://doi.org/10.1038/s41560-018-0191-3.
7. Elmaataouy E, Chari A, El Bendal A, Tayoury M, Amine R, Aqil M, Xu G, Liu T, Alami J, Dahbi M. $LiNi_{0.8}Fe_{0.1}Al_{0.1}O_2$ as a cobalt-free cathode material with high capacity and high capability for lithium-ion batteries. Batteries (Basel). 2023;9:23. https://doi.org/10.3390/batteries9010023.
8. Manthiram A. A reflection on lithium-ion battery cathode chemistry. Nat Commun. 2020;11:1550. https://doi.org/10.1038/s41467-020-15355-0.
9. Liu T, Yu L, Liu J, Lu J, Bi X, Dai A, Li M, Li M, Hu Z, Ma L, Luo D, Zheng J, Wu T, Ren Y, Wen J, Pan F, Amine K. Understanding Co roles towards developing Co-free Ni-rich cathodes for rechargeable batteries. Nat Energy. 2021;6:277–86. https://doi.org/10.1038/s41560-021-00776-y.
10. Li J, Lin C, Weng M, Qiu Y, Chen P, Yang K, Huang W, Hong Y, Li J, Zhang M, Dong C, Zhao W, Xu Z, Wang X, Xu K, Sun J, Pan F. Structural origin of the high-voltage instability of lithium cobalt oxide. Nat Nanotechnol. 2021;16:599–605. https://doi.org/10.1038/s41565-021-00855-x.
11. Bianchini M, Roca-Ayats M, Hartmann P, Brezesinski T, Janek J. There and back again—The journey of $LiNiO_2$ as a cathode active material. Angew Chem Int Ed. 2018;58:10434–58. https://doi.org/10.1002/anie.201812472.
12. Deng T, Fan X, Cao L, Chen J, Hou S, Ji X, Chen L, Li S, Zhou X, Hu E, Su D, Yang XQ, Wang C. Designing in-situ-formed interphases enables highly reversible cobalt-free $LiNiO_2$ cathode for Li-ion and Li-metal batteries. Joule. 2019;3:2550–64.
13. Chien PH, Wu X, Song B, Yang Z, Waters CK, Everett MS, Lin F, Du Z, Liu J. New insights into structural evolution of $LiNiO_2$ revealed by operando neutron diffraction. Batter Supercaps. 2021;4:1701–7. https://doi.org/10.1002/batt.202100135.
14. Mu L, Lin F. Identifying challenges and methods for mitigation in no-cobalt $LiNiO_2$ cathode materials. ECS Meet Abstr. 2020;45:3726. https://doi.org/10.1149/MA2020-02453726mtgabs.
15. Li H, Cormier M, Zhang N, Inglis J, Li J, Dahn JR. Is cobalt needed in Ni-rich positive electrode materials for lithium ion batteries. J Electrochem Soc. 2019;166:A429–39. https://doi.org/10.1149/2.1381902jes.
16. Aishova A, Park GT, Yoon CS, Sun YK. Cobalt-free high-capacity Ni-rich layered $LiNi_{0.9}Mn_{0.1}O_2$ cathode. Adv Energy Mater. 2020;10:1903179. https://doi.org/10.1002/aenm.201903179.
17. Xi Y, Wang M, Xu L, Sari HMK, Li W, Hu J, Cao Y, Chen L, Wang L, Pu X, Wang J, Bai Y, Liu X, Li X. A new Co-free Ni-rich $LiNi_{0.8}Fe_{0.1}Mn_{0.1}O_2$ cathode for low-cost Li ion batteries. ACS Appl Mater Interfaces. 2021;13:57341–9. https://doi.org/10.1021/acsami.1c18303.
18. Muralidharan N, Essehli R, Hermann RP, Parejiya A, Amin R, Bai Y, Du Z, Belharouak I. $LiNi_xFe_yAl_zO_2$, a new cobalt-free layered cathode material for advanced Li-ion batterie. J Power Sour. 2020;471: 228389. https://doi.org/10.1016/j.jpowsour.2020.228389.
19. Li H, Wang L, Song Y, Wu Y, Zhang H, Du A, He X. Understanding the insight mechanism of chemical-mechanical degradation of layered Co-free Ni-rich cathode materials: A review. Nano-Micro Small. 2023;19:2302208. https://doi.org/10.1002/smll.202302208.
20. Ni L, Guo R, Fang S, Chen J, Gao J, Mei Y, Zhang S, Deng W. Crack-free single-crystalline Co-free Ni-rich $LiNi_{0.95}Mn_{0.05}O_2$ layered cathode. eScience. 2022;2:116–24. https://doi.org/10.1016/j.esci.2022.02.006.
21. Shen J, Zhang B, Huang W, Li X, Xiao Z, Wang J, Zhou T, Wen J, Liu T, Amine K, Ou X. Achieving thermodynamic stability of single-crystal Co-free Ni-rich cathode material for high voltage lithium-ion batteries. Adv Func Mater. 2023;33:2300081. https://doi.org/10.1002/adfm.202300081.
22. Kan H, Yang Z, Meng Q, Dong P, Zhang Y. Preparation and electrochemical performance of the Ni-rich Co-free cathode material $LiNi_{0.94}Mn_{0.04}Al_{0.02}O_2$. Energy Fuels. 2024;38:6420–6. https://doi.org/10.1021/acs.energyfuels.3c04759.
23. Li X, Chang K, Abbas SM, El-Tawil RS, Abdel-Ghany AE, Hashem AM, Wang H, Coughlin AL, Zhang S, Mauger A, Zhu L, Julien CM. Silver nanocoating of $LiNi_{0.8}Co_{0.1}Mn_{0.1}O_2$ cathode material for lithium-ion batteries. Micromachines. 2023;14:907. https://doi.org/10.3390/mi14050907.
24. Li Y, Zhu J, Deng S, Lei T, Chen Y, Cao G, Wang S, Zhang J, Guo J. Towards superior cyclability of $LiNi_{0.8}Co_{0.1}Mn_{0.1}O2$ cathode material for lithium ion batteries via synergetic effects of Sb modification. J Alloys Compd. 2019;798798:93–103. https://doi.org/10.1016/j.jallcom.2019.05.217.

25. Liu J, Du Z, Wang X, Tan S, Wu X, Geng L, Song B, Chien PH, Everett SM, Hu E. Anionic redox induced anomalous structural transition in Ni-rich cathodes. Energy Environ Sci. 2021;14:6441–54. https://doi.org/10.1039/d1ee02987h.
26. Zha G, Hu N, Luo Y, Wang F, Wu R, Li Y, Fu H, Fu X. Reducing Ni/Li disorder and boosting electrochemical performance of $LiNi_{0.8}Co_{0.067}Fe_{0.033}Mn_{0.1}O_2$ cathode material. J Taiwan Inst Chem Eng. 2023;144: 104730. https://doi.org/10.1016/j.jtice.2023.104730.
27. Abdel-Ghany AE, Hashem AM, Elzahany EA, Abuzeid HA, Indris S, Nikolowski K, Ehrenberg H, Zaghib K, Mauger A, Julien CM. Structural properties and application in lithium cells of $Li(Ni_{0.5}Co_{0.5})_{1-y}Fe_yO_2$ (0≤y≤0.25) prepared by sol-gel route: Doping optimization. J Power Sour. 2016;320:168–79. https://doi.org/10.1016/j.jpowsour.2016.04.087.
28. Pang WK, Kalluri S, Peterson VK, Doub SX, Guo Z. Electrochemistry and structure of the cobalt-free $Li_{1+x}MO_2$ (M = Li, Ni, Mn, Fe) composite cathode. Phys Chem Chem Phys. 2014;16:25377–85. https://doi.org/10.1039/C4CP02864C.
29. Delmas C, Prado G, Rougier A, Suard E, Fournès L. Effect of iron on the electrochemical behaviour of lithium nickelate: from LiNiO to 2D-$LiFeO_2$. Solid State Ion. 2000;135:71–9. https://doi.org/10.1016/S0167-2738(00)00333-7.
30. Shannon RD, Prewitt CT. Revised values of effective ionic radii. Acta Cryst. 1970;26:1046–8. https://doi.org/10.1107/S0567740870003576.
31. Song MY, Kwon IH. Electrochemical properties of $LiNi_{1-y}Fe_yO_2$ synthesized by the combustion method in O_2. J Alloys Compd. 2009;484:591–6. https://doi.org/10.1016/j.jallcom.2009.04.155.
32. Reimers JN, Rossen E, Jones CD, Dahn JR. Structure and electrochemistry of $Li_xFe_yNi_{1-y}O_2$. Solid State Ion. 1993;61:335–44. https://doi.org/10.1016/0167-2738(93)90401-N.
33. Williamson GK, Hall WH. X-ray line broadening from filed aluminium and wolfram. Acta Metall. 1953;1:22–31. https://doi.org/10.1016/0001-6160(53)90006-6.
34. Tran N, Croguennec L, Jordy C, Biensan P, Delmas C. Influence of the synthesis route on the electrochemical properties of $LiNi_{0.425}Mn_{0.425}Co_{0.15}O_2$. Solid State Ion. 2005;176:1539–47. https://doi.org/10.1016/j.ssi.2005.04.039.
35. Wang H, Hashem AM, Abdel-Ghany AE, Abbas SM, El-Tawil RS, Li T, Li X, El-Mounayri H, Tovar A, Zhu L, Mauger A, Julien CM. Effect of cationic (Na^+) and anionic (F^-) co-doping on the structural and electrochemical properties of $LiNi_{1/3}Mn_{1/3}Co_{1/3}O_2$ cathode material for lithium-ion batteries. Int J Mol Sci. 2023;23:6755. https://doi.org/10.3390/ijms23126755.
36. Prado G, Rougier A, Fournès L, Delmas C. Electrochemical behavior of iron-substituted lithium nickelate. J Electrochem Soc. 2000;147(8):2880–7. https://doi.org/10.1149/1.1393620.
37. Hashem AM, Abdel-Ghany AE, Scheuermann M, Indris S, Ehrenberg H, Mauger A, Julien CM. Doped nanoscale NMC333 as cathode materials for Li-ion batteries. Materials (Basel). 2019;12:2899. https://doi.org/10.3390/ma12182899.
38. Hashem AM, Abdel-Ghany AE, El-Tawil RS, Mauger A, Julien CM. Effect of Na doping on the electrochemicalperformance of $Li_{1.2}Ni_{0.13}Co_{0.13}Mn_{0.54}O_2$ cathode for lithium-ion batteries. Sustain Chem. 2022;3:131–48. https://doi.org/10.3390/suschem3020010.
39. Cui Z, Manthiram A. Thermal stability and outgassing behaviors of high-nickel cathodes in lithium-ion batteries. Angew Chem Int Ed. 2023;62: e202307243. https://doi.org/10.1002/anie.202307243.
40. Li J, Li Y, Guo Y, Lv J, Yi W, Ma P. A facile method to enhance electrochemical performance of highnickel cathode material $Li(Ni_{0.8}Co_{0.1}Mn_{0.1})O_2$ via Ti doping. J Mater Sci Mater Electron. 2018;29:10702–8. https://doi.org/10.1007/s10854-018-9093-1.
41. Ben-Kamel K, Amdouni N, Mauger A, Julien CM. Study of the local structure of $LiNi_{0.33+\delta}Mn_{0.33+\delta}Co_{0.33-2\delta}O_2$ ($0.025 < \delta < 0.075$) oxides. J Alloys Compd. 2012;528:91–8. https://doi.org/10.1016/j.jallcom.2012.03.018.
42. Granados-Miralles C, Serrano A, Prieto P, Guzman-Mínguez J, Prieto JE, Friedel AM, García-Martín E, Fernandez JF, Quesada A. Quantifying Li-content for compositional tailoring of lithium ferrite ceramics. J Eur Ceram Soc. 2023;43:3351–9. https://doi.org/10.1016/j.jeurceramsoc.2023.02.011.
43. Julien C. Local cationic environment in lithium nickel-cobalt oxides used as cathode materials for lithium batteries. Solid State Ion. 2000;136–137:887–96. https://doi.org/10.1016/S0167-2738(00)00503-8.
44. Abdel-Ghany AE, Mauger A, Groult H, Zaghib K, Julien CM. Structural properties and electrochemistry of α-$LiFeO_2$. J Power Sour. 2016;197:285–91. https://doi.org/10.1016/j.jpowsour.2011.09.054.
45. Sotomayor F, Cychosz KA, Thommes M. Characterization of micro/mesoporous materials by physisorption: Concepts and case studies. Acc Mater Surf Res. 2018;3:34–50.
46. Zhao T, Ji R, Meng Y, Zhang G, Si H, Wang Y, Yang M, Wu F, Li L, Chen R. In situ generated spinel-phase skin on layered Li-rich short nanorods as cathode materials for lithium-ion batteries. J Mater Sci. 2019;54:9098–110. https://doi.org/10.1007/s10853-019-03425-8.
47. Zha G, Hu W, Agarwal S, Ouyang C, Hu N, Hou H. High performance layered $LiNi_{0.8}Co_{0.07}Fe_{0.03}Mn_{0.1}O_2$ cathode materials for Li-ion battery. Chem Eng J. 2021;409: 128343. https://doi.org/10.1016/j.cej.2020.128343.
48. Park S, Jo C, Kim HJ, Kim S, Myung ST, Kang HK, Kim H, Song J, Yu J, Kwon K. Understanding the role of trace amount of Fe incorporated in Ni-rich $Li[Ni_{1-x-y}Co_xMn_y]O_2$ cathode material. J Alloys Compd. 2020;835: 155342. https://doi.org/10.1016/j.jallcom.2020.155342.
49. Zheng GT, Xin C, Zhuo Z, Liu J, Li Q, Hu Z, Xu M, Yan S, Yang W, Pan F. Role of superexchange interaction on tuning of Ni/Li disordering in layered $Li(Ni_xMn_yCo_z)O_2$. J Phys Chem Lett. 2017;8:5537–42. https://doi.org/10.1021/acs.jpclett.7b02498.
50. Zheng J, Ye Y, Liu T, Xiao Y, Wang C, Pan F. Ni/Li disordering in layered transition metal oxide: electrochemical impact. Acc Chem Res. 2019;52:2201–9. https://doi.org/10.1021/acs.accounts.9b00033.
51. Ryu HH, Park KJ, Yoon CS, Sun YK. Capacity fading of Ni-rich $Li[Ni_xCo_yMn1_{-x-y}]O_2$ ($0.6 \le x \le 0.95$) cathodes for high-energy-density lithium-ion batteries: bulk or surface degradation. Chem Mater. 2018;30:1155–63. https://doi.org/10.1021/acs.chemmater.7b05269.
52. Zheng S, Hong C, Guan X, Xiang Y, Liu X, Xu GL, Liu R, Zhong G, Zheng F, Li Y, Zhang X, Ren Y, Chen Z, Amine K, Yang Y. Correlation between long range and local structural changes in Ni-rich layered materials during charge and discharge process. J Power Sour. 2019;412:336–43. https://doi.org/10.1016/j.jpowsour.2018.11.053.
53. Hu D, Su Y, Chen L, Li N, Bao L, Lu Y, Zhang Q, Wang J, Chen S, Wu F. The mechanism of side reaction induced capacity fading of Ni-rich cathode materials for lithium ion batteries. J Energy Chem. 2021;58:1–8. https://doi.org/10.1016/j.jechem.2020.09.031.
54. Zheng J, Myeong S, Cho W, Yan P, Xiao J, Wang C, Cho J, Zhang JG, Zheng J, Myeong S, Cho W, Yan P, Xiao J, Wang C, Cho J, Zhang JG. Li- and Mn-rich cathode materials: Challenges to commercialization. Adv Energy Mater. 2017;7:1601284. https://doi.org/10.1002/aenm.201601284.

55. Wilcox J, Patoux S, Doeff M.M, Structure and electrochemistry of $LiNi_{1/3}Co_{1/3-y}M_yMn_{1/3}O_2$ (M=Ti, Al, Fe) positive electrode materials. J Electrochem Soc 2009; 156: A192. https://escholarship.org/uc/item/3c16j847
56. El-Mofid W, Ivanov S, Konkin A, Bund A. A high performance layered transition metal oxide cathode material obtained by simultaneous aluminum and iron cationic substitution. J Power Sour. 2014;268:414. https://doi.org/10.1016/j.jpowsour.2014.06.048.
57. Zhu Z, Gao A, Liang Y, Yi F, Meng T, Ling J, Hao J, Shu D. Dual functional tungsten boosted lithium-ion diffusion and structural integrity of $LiNi_{0.8}Co_{0.1}Mn_{0.1}O_2$ cathodes for high performance lithium-ion batteries. ACS Sustain Chem Eng. 2022;10:50. https://doi.org/10.1021/acssuschemeng.1c04076.
58. Zhang S. S, Problems and their origins of Ni-rich layered oxide cathode materials. Energy Stor Mater. 2020;24:247. https://doi.org/10.1016/j.ensm.2019.08.013.

Publisher's Note